

SCIENTIFIC REPORTS

OPEN

Structural Transformation of Biochar Black Carbon by C₆₀ Superstructure: Environmental Implications

Minori Uchimiya¹, Joseph J. Pignatello², Jason C. White³, Szu-Tung Hu⁴ & Paulo J. Ferreira⁴

Pyrogenic carbon is widespread in soil due to wildfires, soot deposition, and intentional amendment of pyrolyzed waste biomass (biochar). Interactions between engineered carbon nanoparticles and natural pyrogenic carbon (char) are unknown. This study first employed transmission electron microscopy (TEM) and X-ray diffraction (XRD) to interpret the superstructure composing aqueous fullerene C₆₀ nanoparticles prepared by prolonged stirring of commercial fullerite in water (nC₆₀-stir). The nC₆₀-stir was a superstructure composed of face-centered cubic (fcc) close-packing of near-spherical C₆₀ superatoms. The nC₆₀-stir superstructure (≈100 nm) reproducibly disintegrated pecan shell biochar pellets (2 mm) made at 700 °C into a stable and homogeneous aqueous colloidal (<100 nm) suspension. The amorphous carbon structure of biochar was preserved after the disintegration, which only occurred above the weight ratio of 30,000 biochar to nC₆₀-stir. Favorable hydrophobic surface interactions between nC₆₀-stir and 700 °C biochar likely disrupted van der Waals forces holding together the amorphous carbon units of biochar and C₆₀ packing in the nC₆₀ superstructure.

Aqueous fullerene C₆₀ colloids (nC₆₀) prepared by the extended stirring in water or sonication-assisted solvent exchange are frequently considered within the environmental sciences community to be aggregates of individual 60-carbon molecules^{1–7}. For example, Chen and Elimelich⁸ described nC₆₀ as “alignment of C₆₀ molecules”, rather than a new particle or superstructure. Similarly, Murdianti et al.⁵ provided a graphical illustration of nC₆₀ as the homo-aggregate of individual C₆₀ molecules. Choi et al.⁶ emphasized that the interaction of C₆₀ molecules with water controlled the size of the aggregates composed of 60-carbon molecules. Owing to its low aqueous solubility, which is estimated to be ≈2.63 ng L⁻¹ based on toluene extraction^{5,9}, C₆₀ molecules are postulated to form clusters/aggregates at supersaturation⁶ that further combine to form spherical nC₆₀ nanoparticles observable by transmission electron (TEM) and atomic force (AFM) microscopy^{1,2,7}. Under this aggregation model, nC₆₀ is a stable colloid composed of “randomly arranged, individual C₆₀ molecules and their bulk clusters (aggregates)”^{1,7}. However, to our knowledge, individual C₆₀ molecules have not been visualized in aqueous nC₆₀ stock solutions, despite being large enough (≈0.5 nm) to be observed by TEM^{10,11}.

An alternative nC₆₀ formation mechanism is the physical disintegration of large particles into nanometer-sized particles¹². Fullerite (commercially available C₆₀ crystals) forms particles less than 20 nm when hand-ground¹³ or rubbed between the fingertips¹⁴. The resulting fullerite nanoparticles have the same face-centered cubic (fcc) crystal plane as the bulk fullerite powder, and form stable aqueous suspensions¹⁴. The fullerene C₆₀ molecule is a near-perfect sphere categorized as a superatom, i.e., a molecule that acts as a stable unit like an atom¹⁵. Superatomic C₆₀ building blocks self-organize to form a regular secondary hierarchical structure, which is called a superlattice, supercrystal, or superstructure¹⁵. This closely-packed fcc crystal structure of C₆₀ bulk powder (fullerite) has long been recognized^{16–19}. The present study will refer to the fcc crystal structure of nC₆₀ as

¹USDA-ARS Southern Regional Research Center, 1100 Robert E. Lee Boulevard, New Orleans, Louisiana, 70124, USA. ²Department of Environmental Sciences, The Connecticut Agricultural Experiment Station, New Haven, Connecticut, 06504, USA. ³Department of Analytical Chemistry, The Connecticut Agricultural Experiment Station, New Haven, Connecticut, 06504, USA. ⁴Materials Science and Engineering Program, The University of Texas at Austin, Austin, Texas, 78712, USA. Correspondence and requests for materials should be addressed to M.U. (email: sophie.uchimiya@ars.usda.gov)

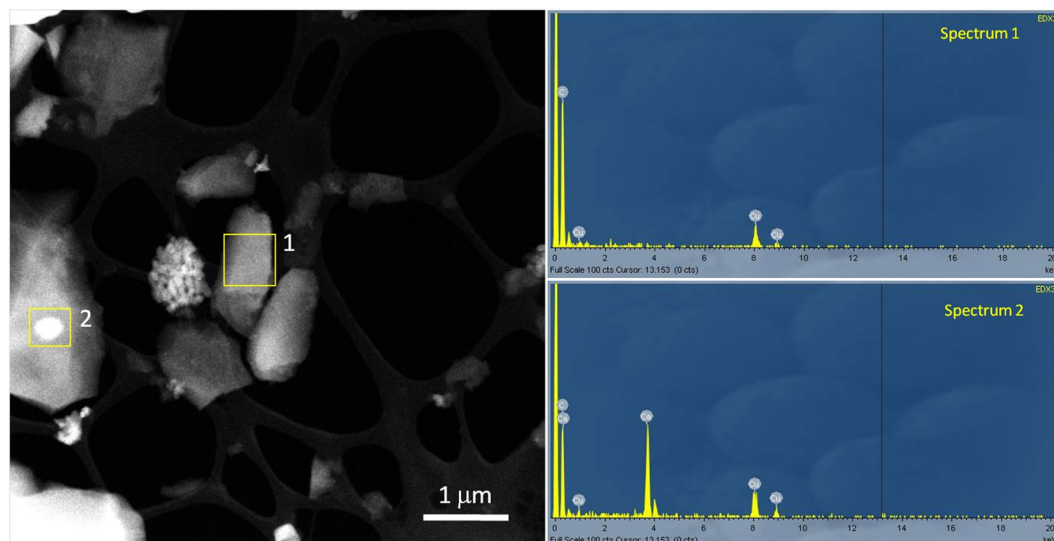


Figure 1. HAADF STEM image and EDS analysis of 700 °C pecan shell biochar. Spectrum 1 acquired from the region within yellow box 1 shows carbon as the only element. Spectrum 2 taken from the bright area within yellow box 2 shows the presence of Ca, C and O. Cu peaks in both spectra are from the TEM grid.

“superstructure” to describe the secondary hierarchical structure formed by the C_{60} superatoms. The C_{60} “superatoms” in the superstructure are held together by weak van der Waals forces^{20,21}.

Previous studies show that the fcc packing of the C_{60} superstructure is preserved in the aqueous nC_{60} formed by sonication of fullerite powder in water (without solvent)²², solvent (toluene or THF) exchange^{22,23}, prolonged stirring¹², or grinding and suspension of the ground material¹⁴. In contrast, highly water soluble fullerol powder ($C_{60}(OH)_x$, $x = 20\text{--}24$) forms a low-density amorphous aggregate/cluster of varying size (100 to >500 nm)²⁴, which is consistent with the aggregation model^{1,2}. Because the concept of C_{60} superatoms and their cohesion to form the nC_{60} superstructure is not well recognized within the environmental sciences community^{3,5,6}, there is a considerable knowledge gap in the environmental behavior of fullerene, including its solubility, formation, mobility, and surface interactions.

The present study employed TEM and X-ray diffraction (XRD) to first demonstrate the fcc superstructure from nC_{60} suspensions prepared by prolonged (40 d) stirring of fullerite in water. Then, batch retention experiments were conducted to investigate the surface interactions between nC_{60} and chars made from pecan shells. Char is a common constituent of soil originating from historical wildfires, land clearing, crop residue burning, or the intentional application of pyrolyzed biomass wastes (biochar)²⁵. Char materials comprise as much as 35% of soil organic carbon²⁶. The projected increase in wildfire²⁷ and intentional biochar soil amendment²⁵ could increase the pyrogenic carbon content of soils. Limited experiments on sludge²⁸, soil^{3,29,30}, and sand³¹ did not report the nC_{60} mass balance. The present study will explore the following potential interaction mechanisms between char and nC_{60} : hydrophobic, van der Waals²⁰, and charge repulsion.

Results and Discussion

TEM imaging of biochar nanostructures. Biochars are hereby denoted by the feedstock acronym and pyrolysis temperature, e.g., pecan shell feedstock (PS25) and biochar produced at 700 °C (PS700). Grand Canonical Monte Carlo (GCMC) density functional theory (DFT) analysis of CO_2 isotherm indicated a progressive increase in the surface area of biochars from 271 to 542 $m^2 g^{-1}$ as a function of pyrolysis temperature (400–700 °C, Table S1). Carbon dioxide measures surface area originating primarily in micropores <1.5 nm in aperture. Because PS700 showed the highest total surface area, TEM was employed to image the nanostructure of PS700.

To probe variations in mass/thickness, high angular annular dark field (HAADF) scanning TEM (STEM) was used, as it is sensitive to the atomic number ($\propto Z^2$)³². In this fashion, regions of PS700 having high Z are brighter under the HAADF STEM contrast, while regions with low Z are darker. Because carbon has a low Z value, an accelerating voltage of 120 keV was employed to increase the scattering cross-section and improve image contrast. As shown in Fig. 1, ball-milled PS700 particles of 1–2 μm in size had regions with darker and brighter contrasts. In Fig. 1, yellow squares indicate two locations where EDS signals were obtained. Spectrum 1 (obtained from a particle without brighter contrast) shows carbon as the only element. Spectrum 2 (obtained from a particle with brighter contrast) is dominated by Ca, C, and O signals. Copper peaks in both spectra originate from the Cu grid. Thus, calcium is the cause for the brighter contrast in the STEM-HAADF image. Phase contrast TEM images confirmed that the presence of Ca is related with crystalline $CaCO_3$ phase³³.

The HAADF STEM is a mass-thickness contrast technique, which is sensitive to variations in thickness, and is used to identify meso- (2–50 nm) and macropores (>50 nm)³². Fig. 2 shows a bright-field STEM image of PS700. Because the carbon is amorphous (shown by Fast Fourier Transform (FFT) in the inset of Fig. 2a), the contrast primarily results from differences in mass/thickness throughout the amorphous carbon. Pores within the

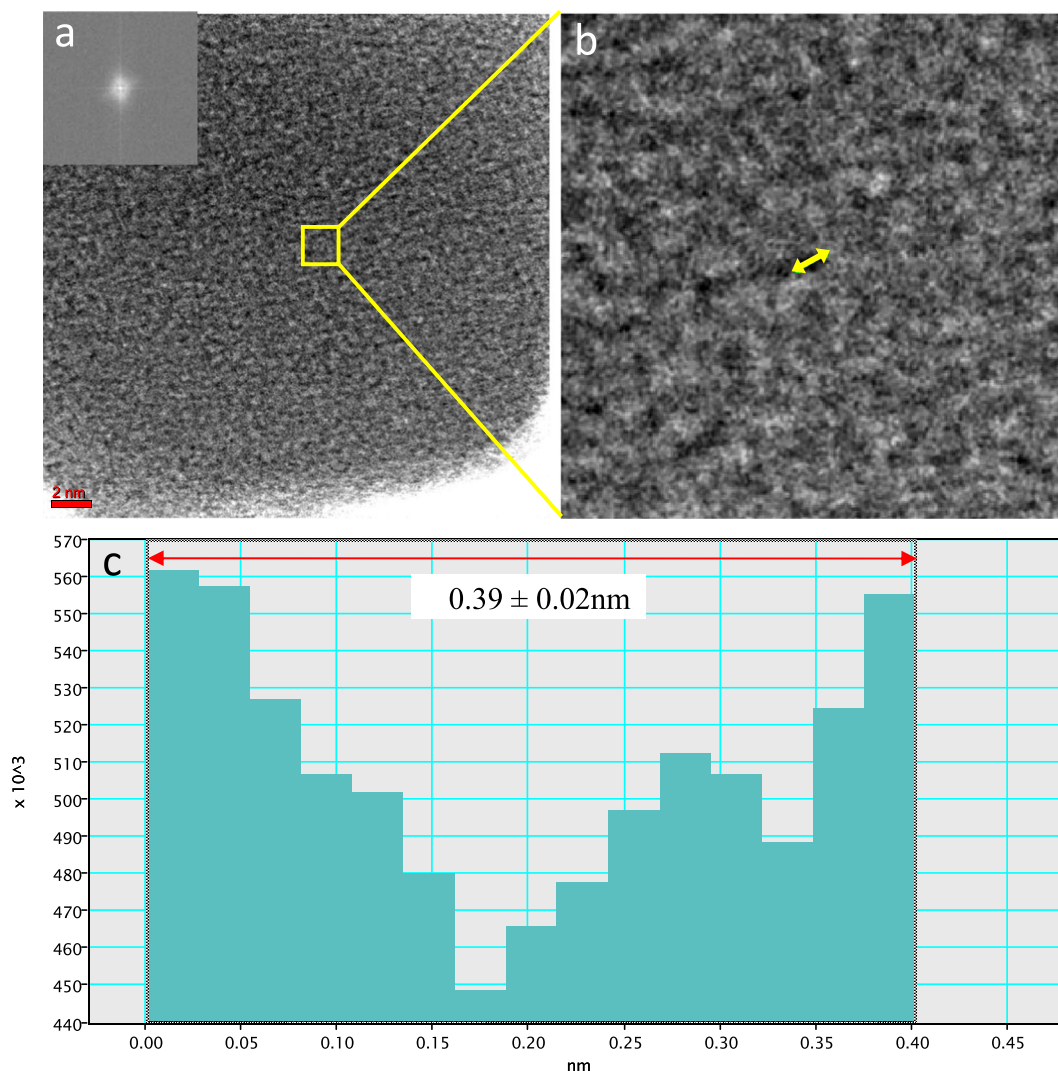


Figure 2. (a) Bright-field STEM image of 700 °C pecan shell biochar. The FFT (shown in the inset) confirms that the carbon is amorphous. (b) Higher magnification image of (a) showing the porosity of the sample (dark spots). (c) Intensity profile across the dark spots (yellow arrow) suggests a pore diameter of approximately 0.39 ± 0.02 nm.

amorphous carbon sample would create a darker contrast in Fig. 2. These dark spots shown in Fig. 2b are likely the locations of micropores measurable by CO₂ GCMC (Table S1). Based on the intensity profile across these regions (described in detail in Section VIII of Supporting Information), the pore diameter was estimated to be approximately 0.39 ± 0.02 nm (Fig. 2c). For the first time, bright-field STEM was employed to visually estimate the size of pores open to the surface of a black carbon material (amorphous carbon of PS700) to be approximately 0.39 ± 0.02 nm.

TEM imaging of nC₆₀-stir superstructure. Bright-field TEM images of nC₆₀-stir show lattice fringes, which indicate the presence of crystallinity (Fig. 3a,b); higher magnification images are provided in Figures S4–S5, Supporting Information. The FFT obtained from Fig. 3b (displayed in the inset) reveals that the nC₆₀-stir exhibits a face-centered-cubic structure with a lattice parameter, $a = 1.356$ nm. To better illustrate this configuration, a model³⁴ is shown in Fig. 3d. Clearly, the nC₆₀-stir is a superstructure formed by C₆₀ near-spheres in a fcc configuration with a lattice parameter of 1.356 nm. To further confirm the superstructure of nC₆₀-stir (Fig. 3c, top spectrum) and fullerite (Fig. 3c, bottom spectrum) were analyzed by XRD. The XRD of nC₆₀-stir shown in Fig. 3c (top spectrum) matched that of fullerite in the XRD database (bottom spectrum). In conclusion, both TEM and XRD analyses indicate that nC₆₀-stir is a superstructure self-assembly of near-spherical C₆₀ molecules in a fcc configuration (Fig. 3d), much like the parent fullerite¹⁶. Although this fcc tendency has been observed in nC₆₀-stir¹², the structural origin has not been explained or interpreted, and was often assumed to be the homo-aggregate of individual C₆₀ molecules^{1–7}. The polydispersity of nC₆₀ superstructure likely controls its dissolution into the toluene extraction fluid used to determine the aqueous “dissolved” C₆₀ concentration, [nC₆₀]_{stock}, as illustrated in the next section.

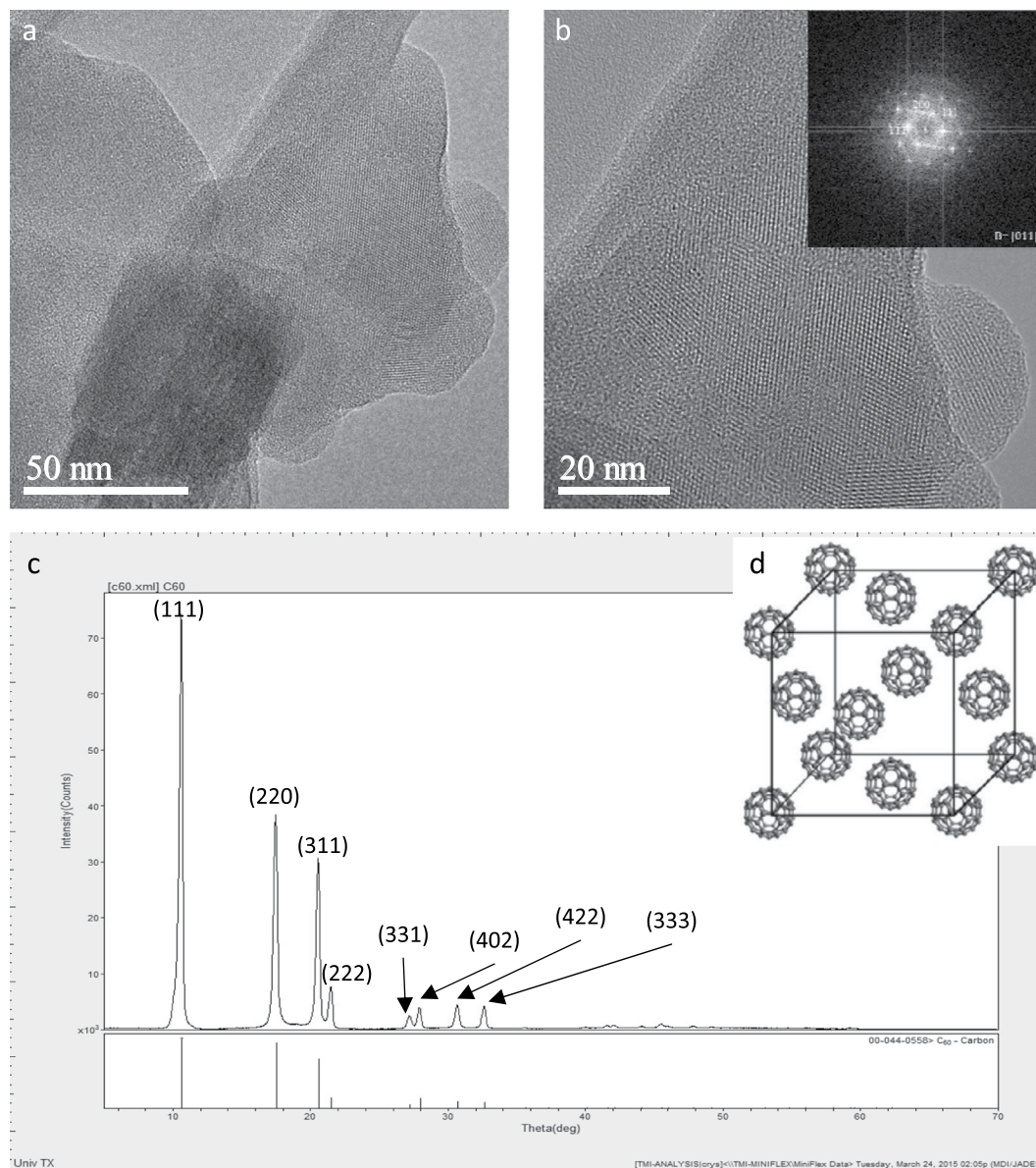


Figure 3. (a) Phase contrast TEM images of nC_{60} -stir. (b) Higher magnification image of a). The FFT shown in the inset indicates a fcc C_{60} superstructure. (c) X-ray diffraction of nC_{60} -stir (top spectrum) and C_{60} template from XRD database (bottom spectrum). (d) Illustrative fcc C_{60} superstructure³⁴.

Characterization of aqueous nC_{60} stock solutions. Prolonged stirring of fullerite in water (to prepare nC_{60} -stir) is intended to simulate the mixing process⁸ taking place in the environment following an accidental spill of fullerite. In previous studies, as summarized in Section VI of Supporting Information, the reproducibility of nC_{60} -stir preparation method had either not been addressed or was called into question^{8,35}. Of four separate batches of nC_{60} -stir prepared to test the reproducibility of production in the present study, only three produced HPLC-detectable nC_{60} -stir (Fig. 4c–e). Although absorbance was low because of the low nC_{60} -stir concentration, two broad peaks were observed at 260–274 and 350 nm (Fig. 4c–e), in agreement with the literature;^{35,36} a baseline shift at 800 nm³⁶ in some prior reports (which is absent in filtered samples) indicates the presence of unfiltered fullerite. In Fig. 4c–e, nC_{60} -stir concentration (by HPLC) and size (by DLS) varied for 3 different batches from 0.10–0.26 $mg L^{-1}$ and 124–223 nm, respectively. As a reference, Fig. 4a shows the UV/visible spectrum of 20 $mg L^{-1}$ C_{60} in toluene corresponding to its HPLC peak.

Because filtration is often used to fractionate nC_{60} into different nm ranges (based on the filter's pore diameter) before experiments^{3,37}, filtered nC_{60} stock solutions were characterized. The thin lines in Fig. 4b (nC_{60} -sonicate), and 4c–4e (separate batches of nC_{60} -stir) show decreased UV/visible absorbance upon syringe filtration (0.45 μm PTFE). In Fig. 4c–e (nC_{60} -stir), the characteristic peaks at 260 and 350 nm disappeared upon filtration. For nC_{60} -sonicate (Fig. 4b), the peaks at 260 and 344 nm remained but were at lower intensity after filtration; the concentration of nC_{60} -sonicate decreased by an order of magnitude, and resulting low count rate (14.3 kcps at 11 attenuation) did not permit a size measurement by DLS. Other syringe filters (0.45 μm cellulose acetate and

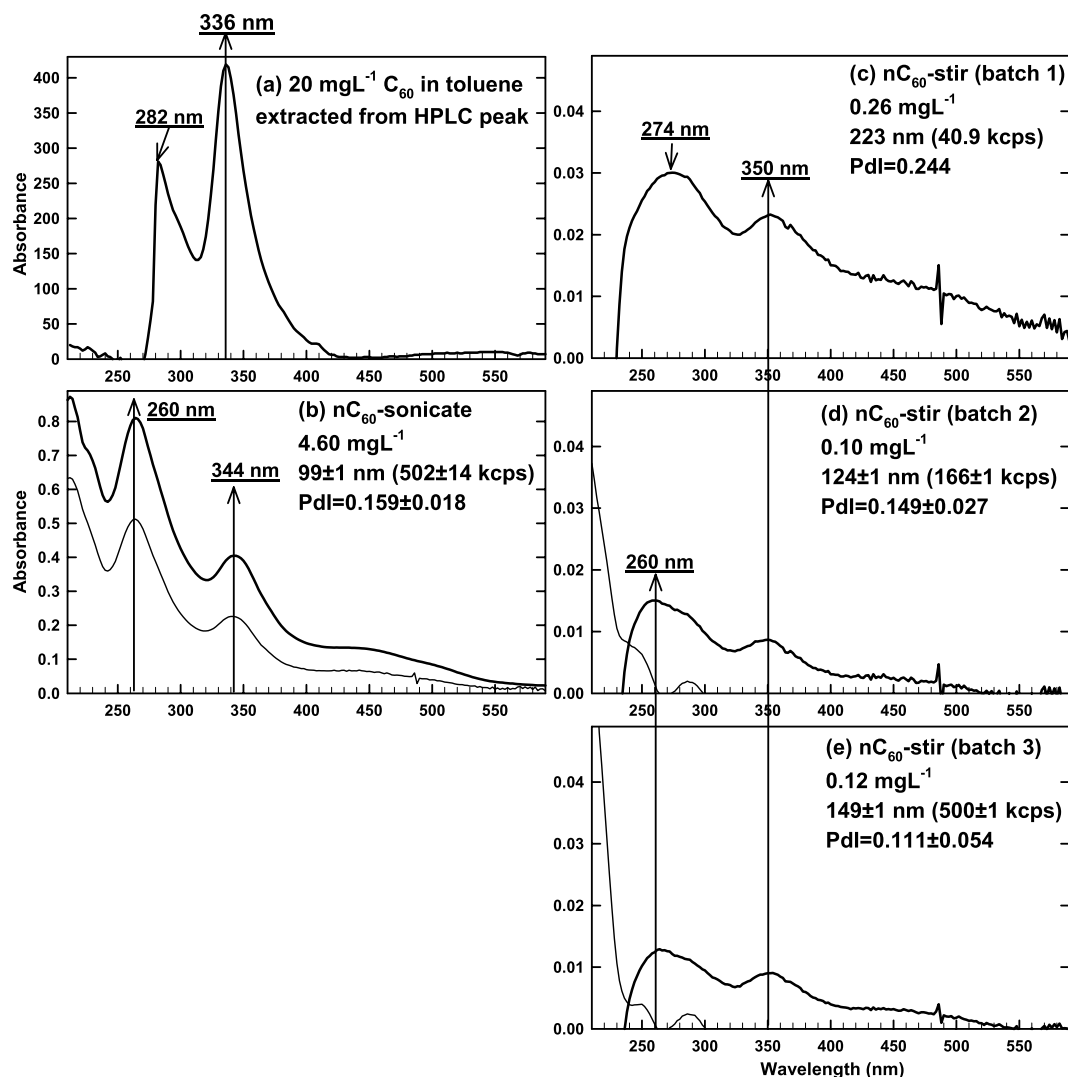


Figure 4. Concentration ($[nC_{60}]_{stock}$ determined by UV-HPLC), size, polydispersity index, count rate (from triplicate DLS analyses), and UV/visible spectra (thin lines were obtained immediately after PTFE syringe filtration) of aqueous nC_{60} stock solutions produced by 40 d magnetic stirring (3 batches in c–e) and sonication (b) in this study. C_{60} dissolved in toluene is shown in (a) as a reference.

nylon, VWR) lead to similar reduction in the absorbance of nC_{60} -sonicate, even though all stock solutions in Fig. 4 had been previously vacuum-filtered through 0.45 μm cellulose acetate membrane filter, as described in the Methods section. Based on above-described influence of syringe filtration, only toluene layer (and not aqueous layer) was filtered prior to the HPLC quantification of C_{60} in the subsequent sections. Above observations suggest that intended size fractionation of nC_{60} via filtration, often employed in the prior reports^{3,37}, could filter out the particles smaller than the filter's pore diameter.

Surface interactions between nC_{60} supercrystals and 2-mm biochar pellets. Figure 5 presents the mass distribution (in μg) of nC_{60} -sonicate (a–b) and nC_{60} -stir (c) in mean \pm s.d. from duplicate retention experiments. In Fig. 5, nC_{60} mass fractions were determined based on $[nC_{60}]_{dissolved}$ for “dissolved” portion of nC_{60} in water at the sampling time, and $[nC_{60}]_{retained}$ for biochar-associated “retained” fraction, as described in detail in Methods section. Mass balance was determined as the sum of dissolved and retained fractions. The “dissolved at $t=0$ ” fraction was based on $[nC_{60}]_{stock}$ measured at each sampling time using the control reactors containing nC_{60} -stir or nC_{60} -sonicate alone, without biochar. Figure 5 in the unit concentration and $[nC_{60}]_{retained,calc}$ (Equation 1) are provided in Figure S6, Supporting Information.

Kinetic experiments were first performed at 5 $g L^{-1}$ PS300 using nC_{60} -sonicate that is an order of magnitude more concentrated than nC_{60} -stir (Fig. 4). As shown in Fig. 5a, dissolved mass of nC_{60} -sonicate remained constant over 1 wk period in the presence of low pyrolysis temperature (300 $^{\circ}C$) biochar. Hot toluene extraction of oven-dried biochar after the retention experiment did not recover nC_{60} -sonicate during the timecourse of the experiment (Fig. 5a). As a result, the C_{60} mass balance (dissolved+retained) equaled the dissolved fraction over 1 wk period.

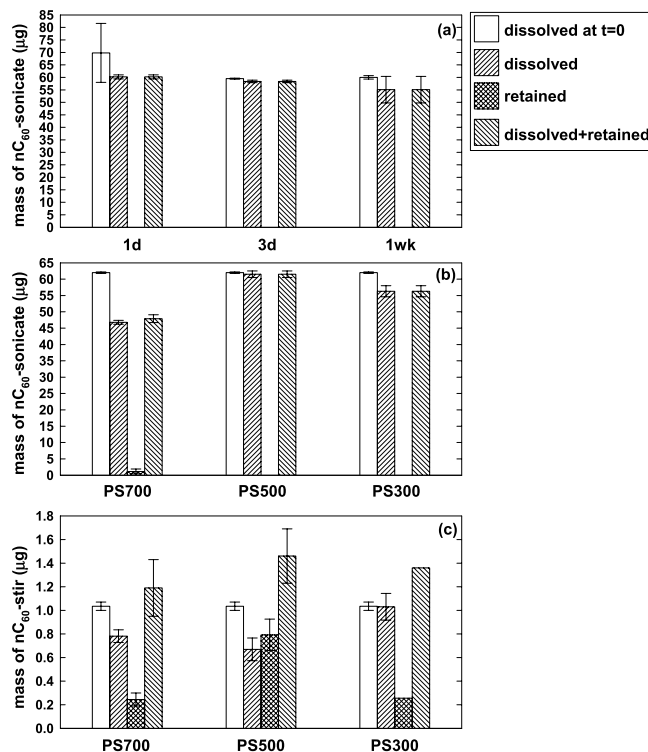


Figure 5. Mass fraction of nC₆₀ (in µg) that was dissolved at t = 0 (calculated based on [nC₆₀]_{stock} of duplicate controls at each sampling time), dissolved at the sampling time (based on [nC₆₀]_{dissolved}), retained on biochar (based on [nC₆₀]_{retained}), and the mass balance (dissolved+retained) from retention kinetics of nC₆₀-sonicate on PS300 (a) and 1 d equilibration of nC₆₀-sonicate (b) and nC₆₀-stir (c) on PS300-700 at 5 (a,c) and 20 g L⁻¹ (b) biochar loadings. All values are given as mean ± s.d. of duplicate experiments.

To investigate the influence of pyrolysis temperature and biochar loading, 1-day equilibration experiment was conducted at a higher loading (20 g L⁻¹) of 300, 500, and 700 °C biochars (Fig. 5b). Higher biochar loading did not significantly decrease the dissolved nC₆₀-sonicate fraction in the presence of PS300 (5–20 g L⁻¹ in Fig. 5a,b). Because of negligibly low solid-associated “retained” fraction, the mass balance of nC₆₀-sonicate was within the error range of the dissolved fraction (PS700 < PS300 < PS500). In conclusion, the retention of nC₆₀-sonicate by 5–20 g L⁻¹ of 300–700 °C biochars was negligibly low. The results in Fig. 5a,b suggest charge repulsion between hydroxyl-enriched nC₆₀-sonicate and carboxyl-enriched PS300; both are negatively charged^{38,39}. Retained fraction of nC₆₀-sonicate was observed only on PS700 (Fig. 5b), which relative to PS300 is more hydrophobic and contains fewer oxygen-containing functional groups^{38,39}.

Figure 5c presents the retention of nC₆₀-stir on 5 g L⁻¹ of 300, 500, and 700 °C biochars. At an order of magnitude lower concentration of nC₆₀-stir than nC₆₀-sonicate, a significant fraction of nC₆₀-stir was retained by biochars in the order, PS300 ≈ PS700 < PS500 (“retained” in Fig. 5c). Dissolved nC₆₀-stir fraction followed the order, PS500 ≈ PS700 < PS300. The mass balance did not show a clear temperature trend, and exceeded the dissolved fraction at t = 0 for PS500 having the highest retained fraction. This could originate from the greater extraction efficiency of nC₆₀-stir from dried biochar (using hot toluene method) than from water. In conclusion, the recovery of nC₆₀-stir retained by the biochar was greater than nC₆₀-sonicate, despite an order of magnitude lower [nC₆₀]_{stock} of nC₆₀-stir than nC₆₀-sonicate. The nC₆₀-sonicate is likely to contain higher amounts of hydroxyl substituent than nC₆₀-stir, because of the sonication process²² incurring radical formation⁴⁰. Favorable hydrophobic interactions between nC₆₀-stir and biochars likely drove the formation of biochar-associated nC₆₀-stir in Fig. 5c.

When high temperature (700 °C) biochar was equilibrated with nC₆₀-stir at a sufficiently high biochar loading (≥20 g biochar L⁻¹), 2-mm biochar pellets reproducibly disintegrated to form a homogeneous, stable, black-colored aqueous colloidal suspension (Fig. 6e). The PS700+nC₆₀-stir suspension (Fig. 6e, far right) was produced at >30,000 biochar/nC₆₀ ratio by weight, and contained measurable [nC₆₀]_{dissolved}. The suspension was stable after the supernatant containing nC₆₀-stir was replaced by water (Figure S7 top far right, Supporting Information). The disintegration of biochar pellets was not observed at lower biochar loadings (Figure S7 top), when low pyrolysis temperature biochar was employed (PS350 in Figure S7, bottom), or when nC₆₀-sonicate was employed instead of nC₆₀-stir. Higher temperature biochars have higher attrition⁴¹ to form smaller particles by mechanical forces^{42,43}. Higher biochar loading could enhance the mechanical crushing of biochar pellets during the end-over-end rotation in the presence of nC₆₀-stir. Hydrophobic interactions between PS700 and nC₆₀-stir (but not nC₆₀-sonicate) lead to the retention of nC₆₀-stir (Fig. 5c) accompanied by the disintegration of biochar (Fig. 6). Collectively, hydrophobic interactions drove the retention of nC₆₀-stir (but not nC₆₀-sonicate having

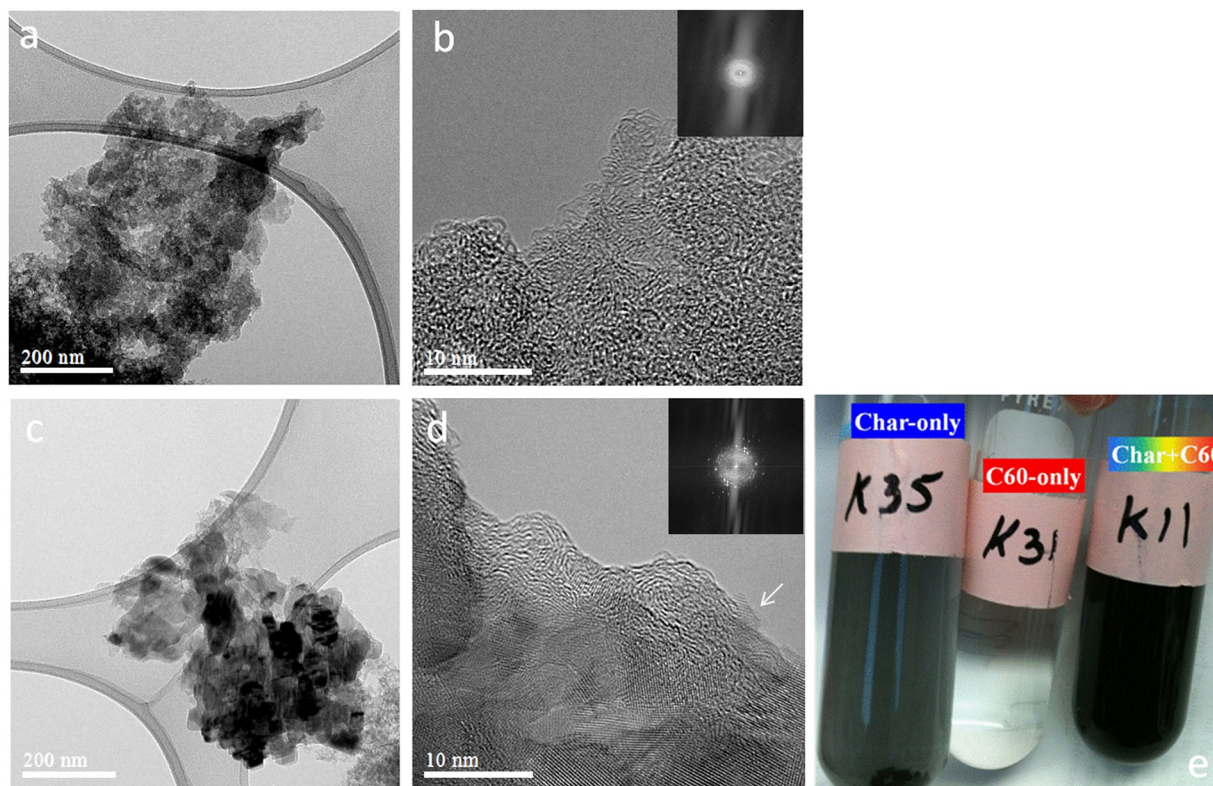


Figure 6. TEM images of PS700+nC₆₀-stir. (a) Amorphous structure. (b) Higher magnification of (a). (c) Crystalline structure. (d) Higher magnification of (c). (e) Disintegration of 2-mm PS700 pellets by nC₆₀-stir after 3 d equilibration (initial conditions: 0.15 g PS700, 0.149 mg L⁻¹ nC₆₀-stir, and 10 mM NaCl). The insets in (b) and (d) confirm the amorphous and crystalline nature of structures.

higher aqueous solubility suggesting greater hydrophilicity, Fig. 4) on biochar, and induced structural transformation of amorphous carbon (PS700) in the presence of crystalline carbon (nC₆₀-stir).

Figure 6a–d show bright-field TEM images of PS700+nC₆₀-stir suspension (6e, far right). Figure 6a,b indicate the formation of amorphous carbon (FFT shown in inset of Fig. 6b) nanoparticles from PS700 pellets, in the presence of nC₆₀-stir. Spaghetti-like amorphous carbon is composed of random carbon domains with defects linked by the aliphatic carbon chains⁴⁴. On the other hand, Fig. 6c,d show a polycrystalline structure composed by nanocrystals having different orientations, as confirmed by multiple diffraction spots (FFT inset of Fig. 6d). However, the lattice spacing was not consistent with the C₆₀ superstructure (Fig. 3), and thus could originate from CaCO₃ in pecan shell biochar (Fig. 1)⁴¹. It is inherently challenging to distinguish two carbon materials (char and C₆₀) by TEM because of low contrast and overlapping projection^{30,45}. However, Fig. 6d shows graphitic structures (arrow) on the edge of amorphous carbon that could originate from the decomposition of nC₆₀-stir superstructure to form C₆₀ molecules. This graphitic structure was not observed in biochar alone (Figs 1, 2) or nC₆₀-stir alone (Fig. 3).

Figure 7a focuses on the polycrystalline structure within the phase contrast TEM image of PS700+nC₆₀-stir. Nanocrystals having different orientations are confirmed by the multiple diffraction spots and lattice fringes in different directions (Fig. 7b is the FFT image of Fig. 7a). By indexing the FFT image, all diffraction rings matched CaCO₃ planes: (102), (104), (113), and (018) towards outer rings in Fig. 7b. However, both yellow and red diffraction spots in Fig. 7b matched the lattice spacing of C₆₀ superstructure: 0.49 nm of (220) plane (red spots in Fig. 7b), and 0.795 nm of (200) plane (yellow spots). In Figures 7c (for yellow spots in Figure 7b) and 7d (for red spots in Figure 7b), an inverse FFT technique was employed to visualize the retained fraction of nC₆₀-stir in PS700. As shown in Fig. 7, the inverse FFT on the red and yellow diffraction spots revealed the C₆₀ superstructures embedded within PS700, i.e., [nC₆₀]_{retained}.

In conclusion, Figs 4–7 re-emphasize that nC₆₀ is a superstructure, rather than the homo-aggregate of C₆₀ molecules. If nC₆₀ was the aggregate of individual C₆₀ molecules, penetration into microporous networks is expected. Such reaction is expected to be highly irreversible, and will be controlled by the abundance of micropores (<2 nm)^{46,47}, which progressively increases from 400 to 700 °C (Table S1). In contrast, van der Waals and hydrophobic interactions involving the polyaromatic surface of PS700 will favor the heteroaggregation of nC₆₀ superstructure. Biochar's hydrophobicity progressively increases as a function of pyrolysis temperature, resulting in the lower H/C atomic ratio (Table S1). Heteroaggregation of nC₆₀-stir with PS700 (Fig. 5c) and associated hydrophobic interactions could disrupt the relatively weak van der Waals forces holding together (i) amorphous carbon units⁴⁴ of biochar and (ii) C₆₀ packing of nC₆₀ superstructure^{20,21,48}.

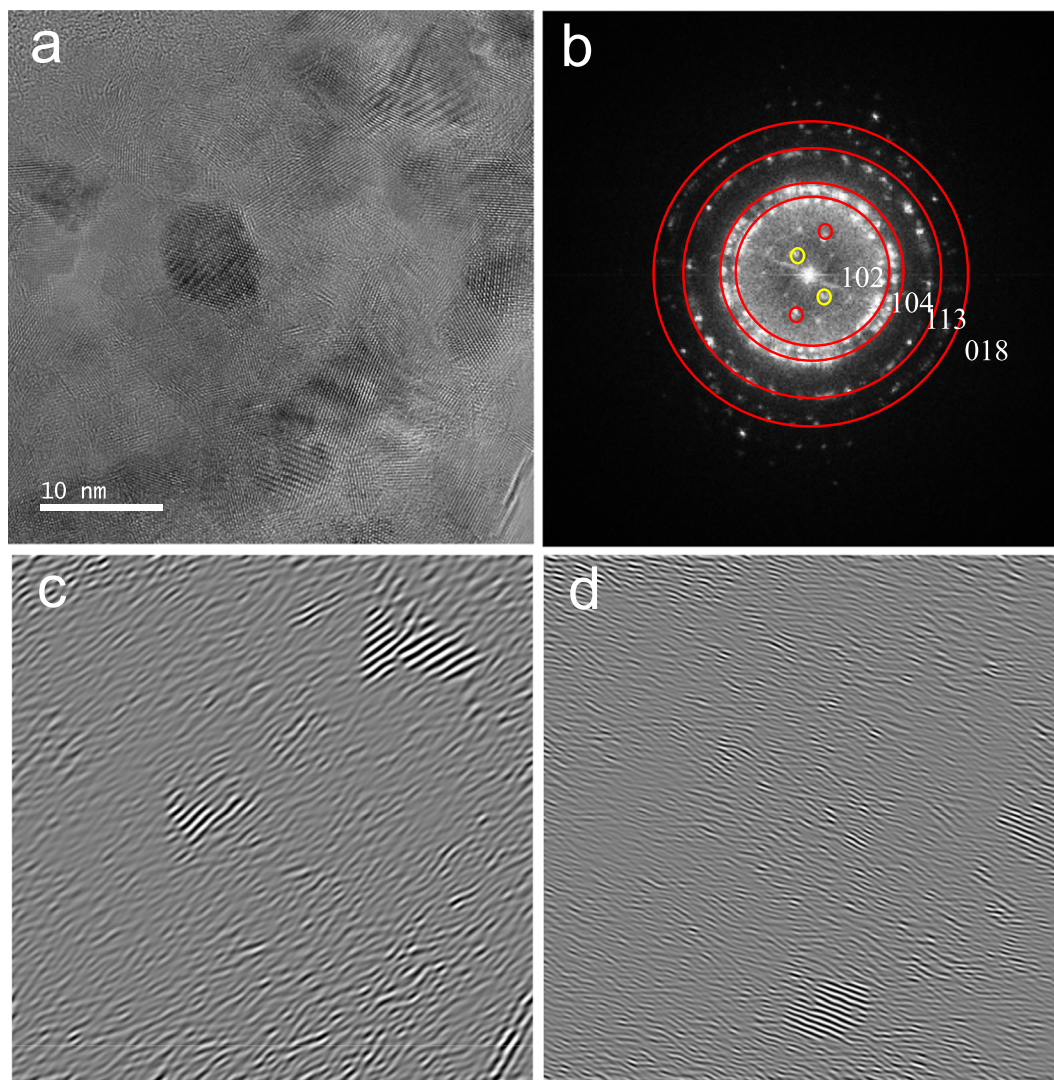


Figure 7. (a) Phase contrast TEM image of C60 superstructure in nC60+PS700. (b) FFT of image (a) showing the presence of CaCO₃ represented by the diffraction rings and the C60 superstructure defined by the yellow and red diffraction spots. (c) Inverse FFT produced by the (200) yellow diffraction spots of the C60 superstructure. (d) Inverse FFT produced by the (220) red diffraction spots of the C60 superstructure.

Physical disintegration of biochar particle by the engineered carbon nanomaterial (nC₆₀; Fig. 6) without sonication⁴⁹, will pose a number of environmental consequences. Environmental transport of pyrogenic carbon is strongly size-dependent⁵⁰, and constitutes a significant proportion of the global carbon cycle⁵¹. The presence of hydrophobic carbon nanoparticles, like nC₆₀-stir occurring from accidental spill, will promote the transport of biochar soil amendment⁵² by producing biochar nanoparticles (Fig. 6) and composites (Fig. 7). Produced biochar nanoparticles will have additional environmental consequences⁵³, including the off-site migration of sorbed pollutants²⁵.

Methods

Distilled, deionized water (DDW) with a resistivity of 18 MΩ cm (APS Water Services, Van Nuys, CA) was used in all procedures. Unless otherwise noted, all chemical reagents were obtained from Sigma-Aldrich (Milwaukee, WI) at the highest purity available.

Pecan shell biochars. As described in detail previously^{49,54}, pecan shell feedstock (PS25) was ground (SM 2000 cutting mill, Retsch GmbH, Haan, Germany) and sieved (<2 mm) prior to pyrolysis at 300, 350, 400, 500, 600, or 700 °C under a flow rate of 1,600 mL min⁻¹ N₂ for 4 h using a laboratory scale box furnace (22 L void volume) with a retort (Lindberg, Type 51662-HR, Watertown, WI). Biochar products were allowed to cool to room temperature overnight under the N₂ atmosphere. Proximate and ultimate analysis results⁵⁴ and N₂ and CO₂ isotherms-based surface area and porosity are summarized in Table S1 of Supporting Information.

Aqueous nC₆₀ stock solutions. Two published methods were used. In the first^{8,55,56}, bulk fullerene C₆₀ powder (99.9% purity fullerite; Materials and Electrochemical Research, Tucson, AZ) was magnetically stirred in DDW (1.0 g L⁻¹) in the dark for 40 d. The suspension was initially black and gradually turned brown over the 40 d stirring period. The suspended particles were removed by the vacuum filtration (DDW pre-rinsed 0.2 μm cellulose acetate membrane; Sartorius, Bohemia, NY) to produce a clear stock solution having a light yellow/brown hue and a pH of 6.0 (Sartorius Professional meter PP-15). The resulting stock solution is denoted nC₆₀-stir. The second method⁵⁷ employed a sonication probe (450 Sonifier, Branson Ultrasonics, Danbury, CT) to increase the nC₆₀ concentration by the oxidative formation of hydroxyl substituents^{22,37}. Five mL of C₆₀ powder dissolved in toluene (1.2 g L⁻¹ clear purple solution) was added to a solution composed of 50 mL DDW and 1.5 mL ethanol. Figure S1 of Supporting Information shows the resulting solution having toluene (top) and aqueous (bottom) layers⁵⁸. This solution was sonicated by directly inserting the probe for 3 h while periodically adding DDW to replace the water evaporated as a result of the exothermic sonication process. Sonication caused the solution to develop a cloudy yellow-white color (Figure S2), and the final solution (after toluene was driven off by the heating) was clear yellow. This solution was vacuum filtered through 0.45 μm (cellulose acetate) and then 0.2 μm (cellulose nitrate) membrane filters. The resulting stock solution is denoted nC₆₀-sonicate (Figure S3). An analogous procedure was followed to produce nC₇₀ stock solution by sonication (nC₇₀-sonicate characterized in the Section VII of Supporting Information) to use as the internal standard in HPLC quantification of nC₆₀. All aqueous fullerene stock solutions (nC₆₀-stir, nC₆₀-sonicate, and nC₇₀-sonicate) were stored at 25 °C in the dark, and were stable for several months, as reported in the literature⁵⁹. The stock solutions were characterized by UV/visible spectrophotometry (HP8452A, Hewlett-Packard, Palo Alto, CA) with DDW as the blank. Hydrodynamic diameter was determined by dynamic light scattering (DLS; Zetasizer NanoZS, Malvern, Westborough, MA). All DLS analyses were performed in triplicate using the disposable sizing cuvette at the material RI of 2.20, attenuation of 11, water as the dispersant, and by the default general method algorithm; count rate (in kcps) and polydispersity index (PDI) were recorded in addition to the hydrodynamic diameter.

Surface interaction of nC₆₀ with biochars. Batch experiments were conducted in duplicate using amber glass vials with Teflon-lined screw caps (40 mL nominal volume, Thermo Fisher Scientific, Waltham, MA) at 5–20 g biochar L⁻¹; 30 mL of undiluted nC₆₀ stock solution was added directly to dry 2-mm biochar pellets. Reactors were equilibrated by shaking end-over-end at 70 rpm. Control experiments were conducted for the nC₆₀ stock solution without biochar, and biochar without nC₆₀ stock solution, each in duplicate. At each sampling time, biochar was allowed to settle for 1 h, and then the supernatant was carefully decanted into a new glass vial. The supernatant was mixed with 200 g L⁻¹ NaCl stock solution to yield 1 wt% NaCl. The NaCl was used to facilitate the transfer of nC₆₀ from the aqueous to toluene phase, and to prevent emulsion⁹. After vigorous shaking by hand, 4 mL toluene (HPLC grade) was added, and the reactor was vortexed and then rotated at 70 rpm overnight. After allowing the two (water and toluene) layers to separate, only the toluene layer was syringe filtered (0.45 μm Millipore Millex-GS; Millipore, Billerica, MA), and 200 μL filtrate was injected into HPLC system with diode array detector (Agilent Technologies, Santa Clara, CA) and Cosmosil Buckyprep-M Packed column (4.6 × 2500 mm; SES Research, Houston, TX). The HPLC column was designed to separate C₆₀ from C₇₀ in pure toluene mobile phase at 1.0 mL min⁻¹ flow rate, and C₆₀ was quantified at λ_{max} of 336 nm in toluene (Fig. 4a) and the retention time of 8 min⁶⁰. Determined nC₆₀ concentration is hereby denoted [nC₆₀]_{dissolved}. The same procedure was used to determine C₆₀ concentrations in nC₆₀-stir and nC₆₀-sonicate stock solutions hereby termed [nC₆₀]_{stock}.

The portion of nC₆₀ retained by biochar (hereby termed [nC₆₀]_{retained}) was independently quantified by a hot toluene extraction method⁶¹. Biochar remaining in each reactor (after decanting supernatant; residual supernatant was determined gravimetrically) was transferred to a clean vial using DDW, and then oven-dried at 45 °C overnight. After recording the weight of oven-dried biochar in the new vial, 2 mL toluene was added, and the resulting biochar suspension in toluene was immersed in 65 °C water bath for 6 h. The reactor was vortexed and rotated at 70 rpm overnight, and then syringe filtered (0.45 μm) for the HPLC analysis of C₆₀, as described above. Solid-associated nC₆₀ was also calculated as [nC₆₀]_{retained,calc} (in mg g⁻¹) using the equation below, and compared with [nC₆₀]_{retained}.⁶²

$$[\text{nC}_{60}]_{\text{retained,calc}} = \frac{V_s}{m}([\text{nC}_{60}]_{\text{stock}} - [\text{nC}_{60}]_{\text{dissolved}}) \quad (1)$$

where V_s is the total volume (30 mL), and m (in g) is the dry weight of 2-mm biochar pellets.

To determine the portion of nC₆₀ retained by the reactor (hereby termed [nC₆₀]_{vial}), both the vial and cap of the amber glass reactor were washed thoroughly 3 times with DDW to remove residual supernatant containing nC₆₀. Washed reactors were air dried, and then 2 mL toluene was added. The capped reactor was then vortexed and rotated at 70 rpm overnight, and then syringe filtered (0.45 μm) for the HPLC analysis. The resulting [nC₆₀]_{vial} was determined to be negligible for all experiments presented in this study.

In each experiment, mass balance (in μg C₆₀) was calculated based on [nC₆₀]_{dissolved} (solution-phase nC₆₀ concentration at the sampling time) and [nC₆₀]_{retained}. The mass balance was compared with μg of nC₆₀ added to each reactor at $t = 0$, which was calculated based on the reactor volume (30 mL) and [nC₆₀]_{stock} determined at each sampling time using the controls containing nC₆₀ stock solution without biochar.

TEM imaging of nC₆₀-stir and biochar before and after the reaction. Ball-milled and sieved (400 mesh, <37 μm) PS700 was sonicated in ethanol for 15 min. One drop of the resulting suspension was deposited on a 200 mesh carbon-lacey Cu grid. To prepare samples containing nC₆₀-stir, two drops of nC₆₀-stir before and after the reaction with PS700 were deposited on the grids. TEM images were obtained using a JEOL 2010F TEM (JEOL USA, Peabody, MA) operated at 120 kV, coupled with an energy-dispersive x-ray spectroscopy (EDS). As

widely described in the literature, TEM observations could modify the structure of aqueous colloids if exposed to high acceleration voltages¹⁰, drying or addition of surfactants/solvents during sample preparation⁶³, or by freezing employed during the cryogenic TEM. With this in mind, the present study employed 120 kV and short exposure times to minimize these experimental artifacts.

X-ray diffraction. The crystalline structures of nC₆₀-stir stock solution and the bulk fullerite powder were characterized by X-ray diffraction (XRD) with a Philips X'pert diffractometer (with Cu K α radiation) using a step-scan mode in the range of 10° to 110° with intervals of 0.03° and wavelength of 1.5406 Å (Cu K α). XRD computer simulations were carried out using a Diamond 3.2e2 software.

References

- Voronin, D. P. *et al.* Evidence of entropically driven C₆₀ fullerene aggregation in aqueous solution. *J. Chem. Phys.* **140**, 104909 (2014).
- Prylutskiy, Y. I. *et al.* C₆₀ fullerene aggregation in aqueous solution. *Phys. Chem. Chem. Phys.* **15**, 9351–9360 (2013).
- Avanasi, R., Jackson, W. A., Sherwin, B., Mudge, J. F. & Anderson, T. A. C₆₀ fullerene soil sorption, biodegradation, and plant uptake. *Environ. Sci. Technol.* **48**, 2792–2797 (2014).
- Fortner, J. D. *et al.* Reaction of water-stable C₆₀ aggregates with ozone. *Environ. Sci. Technol.* **41**, 7497–7502 (2007).
- Murdianti, B. S. *et al.* C₆₀ oxide as a key component of aqueous C₆₀ colloidal suspensions. *Environ. Sci. Technol.* **46**, 7446–7453 (2012).
- Choi, J. I., Snow, S. D., Kim, J.-H. & Jang, S. S. Interaction of C₆₀ with water: first-principles modeling and environmental implications. *Environ. Sci. Technol.* **49**, 1529–1536 (2015).
- Prylutskiy, Y. I. *et al.* On the origin of C₆₀ fullerene solubility in aqueous solution. *Langmuir* **30**, 3967–3970 (2014).
- Chen, K. L. & Elimelech, M. Relating colloidal stability of fullerene (C₆₀) nanoparticles to nanoparticle charge and electrokinetic properties. *Environ. Sci. Technol.* **43**, 7270–7276 (2009).
- Wang, C., Shang, C. & Westerhoff, P. Quantification of fullerene aggregate nC₆₀ in wastewater by high-performance liquid chromatography with UV-vis spectroscopic and mass spectrometric detection. *Chemosphere* **80**, 334–339 (2010).
- Chuvilin, A., Kaiser, U., Bichoutskaia, E., Besley, N. A. & Khlobystov, A. N. Direct transformation of graphene to fullerene. *Nat. Chem.* **2**, 450–453 (2010).
- Khlobystov, A. N., Britz, D. A. & Briggs, G. A. D. Molecules in carbon nanotubes. *Acc. Chem. Res.* **38**, 901–909 (2005).
- Duncan, L. K., Jinschek, J. R. & Vikesland, P. J. C₆₀ colloid formation in aqueous systems: Effects of preparation method on size, structure, and surface charge. *Environ. Sci. Technol.* **42**, 173–178 (2008).
- Deguchi, S., Mukai, S. A., Tsudome, M. & Horikoshi, K. Facile generation of fullerene nanoparticles by hand-grinding. *Adv. Mater.* **18**, 729–732 (2006).
- Deguchi, S., Mukai, S. A., Sakaguchi, H. & Nonomura, Y. Non-engineered nanoparticles of C₆₀. *Sci. Rep.* **3**, 2094 (2013).
- Claridge, S. A. *et al.* Cluster-assembled materials. *ACS Nano* **3**, 244–255 (2009).
- David, W. I. F. *et al.* Crystal structure and bonding of ordered C₆₀. *Nature* **353**, 147–149 (1991).
- Kroto, H. W., Heath, J. R., O'Brien, S. C., Curl, R. F. & Smalley, R. E. C₆₀: Buckminsterfullerene. *Nature* **318**, 162–163 (1985).
- Guo, Y., Karasawa, N. & Goddard III, W. A. Prediction of fullerene packing in C₆₀ and C₇₀ crystals. *Nature* **351**, 464–467 (1991).
- Zhao, J., Feng, M., Yang, J. & Petek, H. The superatom states of fullerenes and their hybridization into the nearly free electron bands of fullerites. *ACS Nano* **3**, 853–864 (2009).
- Saito, S. & Oshiyama, A. Cohesive mechanism and energy bands of solid C₆₀. *Phys. Rev. Lett.* **66**, 2637–2640 (1991).
- Lu, J. P., Li, X. P. & Martin, R. M. Ground state and phase transitions in solid C₆₀. *Phys. Rev. Lett.* **68**, 1551–1554 (1992).
- Labille, J. *et al.* Hydration and dispersion of C₆₀ in aqueous systems: The nature of water-fullerene interactions. *Langmuir* **25**, 11232–11235 (2009).
- Fortner, J. D. *et al.* C₆₀ in water: Nanocrystal formation and microbial response. *Environ. Sci. Technol.* **39**, 4307–4316 (2005).
- Brant, J. A., Labille, J., Robichaud, C. O. & Wiesner, M. Fullerol cluster formation in aqueous solutions: Implications for environmental release. *J. Colloid Interf. Sci.* **314**, 281–288 (2007).
- Pignatello, J. J., Uchimiya, M., Abiven, S. & Schmidt, M. W. I. Evolution of Black Carbon Properties in Soil in *Biochar for Environmental Management: Science, Technology, and Implementation* (J. Lehmann & S. Joseph) 195–234 (Taylor & Francis, 2015).
- Skjemstad, J. O., Reicosky, D. C., Wilts, A. R. & McGowan, J. A. Charcoal carbon in US agricultural soils. *Soil Sci. Soc. Am. J.* **66**, 1249–1255 (2002).
- Flannigan, M. D., Krawchuk, M. A., De Groot, W. J., Wotton, B. M. & Gowman, L. M. Implications of changing climate for global wildland fire. *Int. J. Wildland Fire* **18**, 483–507 (2009).
- Yang, Y., Nakada, N. & Tanaka, H. Adsorption of fullerene nC₆₀ on activated sludge: Kinetics, equilibrium and influencing factors. *Chem. Eng. J.* **225**, 365–371 (2013).
- Forouzangohar, M. & Kookana, R. S. Sorption of nano-C₆₀ clusters in soil: Hydrophilic or hydrophobic interactions? *J. Environ. Monit.* **13**, 1190–1194 (2011).
- Li, D., Lyon, D. Y., Li, Q. & Alvarez, P. J. J. Effect of soil sorption and aquatic natural organic matter on the antibacterial activity of a fullerene water suspension. *Environ. Toxicol. Chem.* **27**, 1888–1894 (2008).
- Chen, K. L. & Elimelech, M. Interaction of fullerene (C₆₀) nanoparticles with humic acid and alginate coated silica surfaces: Measurements, mechanisms, and environmental implications. *Environ. Sci. Technol.* **42**, 7607–7614 (2008).
- Zhu, Y. *et al.* Carbon-based supercapacitors produced by activation of graphene. *Science* **332**, 1537–1541 (2011).
- Uchimiya, M., Pignatello, J. J., White, J. C., Hu, S. & Ferreira, P. J. Surface interactions between gold nanoparticles and biochar. *Sci. Rep.* **7**, 5027 (2017).
- Álvarez-Murga, M. & Hodeau, J. L. Structural phase transitions of C₆₀ under high-pressure and high-temperature. *Carbon* **82**, 381–407 (2015).
- Chang, X. & Vikesland, P. J. Uncontrolled variability in the extinction spectra of C₆₀ nanoparticle suspensions. *Langmuir* **29**, 9685–9693 (2013).
- Chang, X. & Vikesland, P. J. UV-vis spectroscopic properties of nC₆₀ produced via extended mixing. *Environ. Sci. Technol.* **45**, 9967–9974 (2011).
- Chae, S. R. *et al.* Heterogeneities in fullerene nanoparticle aggregates affecting reactivity, bioactivity, and transport. *ACS Nano* **4**, 5011–5018 (2010).
- Xiao, F. & Pignatello, J. J. Interactions of triazine herbicides with biochar: Steric and electronic effects. *Water Res.* **80**, 179–188 (2015).
- Leblanc, J., Uchimiya, M., Ramakrishnan, G., Castaldi, M. J. & Orlov, A. Across-phase biomass pyrolysis stoichiometry, energy balance, and product formation kinetics. *Energ. Fuel* **30**, 6537–6546 (2016).
- Radziuk, D. *et al.* Ultrasound-assisted fusion of preformed gold nanoparticles. *J. Phys. Chem. C* **114**, 1835–1843 (2010).
- Jones, K. *et al.* Fate of higher-mass elements and surface functional groups during the pyrolysis of waste pecan shell. *Energ. Fuel* **29**, 8095–8101 (2015).
- ASTM. Standard Guide for Dusting Attrition of Granular Activated Carbon. (American Society for Testing and Materials, West Conshohocken, PA ASTM D5159, 2014).

43. Sigmund, G. *et al.* Cytotoxicity of biochar: A workplace safety concern? *Environ. Sci. Technol. Lett.*, in press (2017).
44. Ye, R. *et al.* Coal as an abundant source of graphene quantum dots. *Nat. Commun.* **4**, 2943 (2013).
45. Britz, D. A. & Khlbystov, A. N. Noncovalent interactions of molecules with single walled carbon nanotubes. *Chem. Soc. Rev.* **35**, 637–659 (2006).
46. Xiao, F. & Pignatello, J. J. Effects of post-pyrolysis air oxidation of biomass chars on adsorption of neutral and ionizable compounds. *Environ. Sci. Technol.* **50**, 6276–6283 (2016).
47. Braida, W. J. *et al.* Sorption hysteresis of benzene in charcoal particles. *Environ. Sci. Technol.* **37**, 409–417 (2003).
48. Moriarty, P. Nanostructured materials. *Rep. Prog. Phys.* **64**, 297–381 (2001).
49. Yi, P., Pignatello, J. J., Uchimiya, M. & White, J. C. Heteroaggregation of cerium oxide nanoparticles and nanoparticles of pyrolyzed biomass. *Environ. Sci. Technol.* **49**, 13294–13303 (2015).
50. Wang, D., Zhang, W., Hao, X. & Zhou, D. Transport of biochar particles in saturated granular media: Effects of pyrolysis temperature and particle size. *Environ. Sci. Technol.* **47**, 821–828 (2013).
51. Jaffé, R. *et al.* Global charcoal mobilization from soils via dissolution and riverine transport to the oceans. *Science* **340**, 345–347 (2013).
52. Wang, C., Walter, M. T. & Parlange, J. Y. Modeling simple experiments of biochar erosion from soil. *J. Hydrol.* **499**, 140–145 (2013).
53. Valsami-Jones, E. & Lynch, I. How safe are nanomaterials? *Science* **350**, 388–389 (2015).
54. Uchimiya, M. Influence of pH, ionic strength, and multidentate ligand on the interaction of Cd^{II} with biochars. *ACS Sustainable Chem. Eng.* **2**, 2019–2027 (2014).
55. Cheng, X., Kan, A. T. & Tomson, M. B. Naphthalene adsorption and desorption from aqueous C₆₀ fullerene. *J. Chem. Eng. Data* **49**, 675–683 (2004).
56. Jakubczyk, D. *et al.* Study of microscopic properties of water fullerene suspensions by means of resonant light scattering analysis. *J. Phys. D: Appl. Phys.* **37**, 2918–2924 (2004).
57. Chen, K. L. & Elimelech, M. Aggregation and deposition kinetics of fullerene (C₆₀) nanoparticles. *Langmuir* **22**, 10994–11001 (2006).
58. Isaacson, C., Zhang, W., Powell, T., Ma, X. & Bouchard, D. Temporal changes in aqu/C₆₀ physical-chemical, deposition, and transport characteristics in aqueous systems. *Environ. Sci. Technol.* **45**, 5170–5177 (2011).
59. Song, M. *et al.* Size-dependent toxicity of nano-C₆₀ aggregates: More sensitive indication by apoptosis-related bax translocation in cultured human cells. *Environ. Sci. Technol.* **46**, 3457–3464 (2012).
60. Xiao, Y., Chae, S. R. & Wiesner, M. R. Quantification of fullerene (C₆₀) in aqueous samples and use of C₇₀ as surrogate standard. *Chem. Eng. J.* **170**, 555–561 (2011).
61. D L Torre-Roche, R. *et al.* Fullerene-enhanced accumulation of p, p'-DDE in agricultural crop species. *Environ. Sci. Technol.* **46**, 9315–9323 (2012).
62. Kan, A. T., Fu, G. & Tomson, M. B. Adsorption/desorption hysteresis in organic pollutant and soil/sediment interaction. *Environ. Sci. Technol.* **28**, 859–867 (1994).
63. Michen, B. *et al.* Avoiding drying-artifacts in transmission electron microscopy: Characterizing the size and colloidal state of nanoparticles. *Sci. Rep.* **5** (2015).

Acknowledgements

This research was funded by a grant from the U.S. Department of Agriculture, NIFA Agricultural Food Research Initiative, Nanotechnology in Food and Agriculture program, Award No. 2012–67021–19300. Mention of trade names or commercial products in this publication is solely for the purpose of providing specific information and does not imply recommendation or endorsement by the U.S. Department of Agriculture. USDA is an equal opportunity provider and employer.

Author Contributions

M.U. wrote the manuscript. M.U., J.J.P. and J.C.W. planned and directed the experiments. S.-T.H. and P.F. performed and interpreted the microscopy.

Additional Information

Supplementary information accompanies this paper at <https://doi.org/10.1038/s41598-017-12117-9>.

Competing Interests: The authors declare that they have no competing interests.

Publisher's note: Springer Nature remains neutral with regard to jurisdictional claims in published maps and institutional affiliations.



Open Access This article is licensed under a Creative Commons Attribution 4.0 International License, which permits use, sharing, adaptation, distribution and reproduction in any medium or format, as long as you give appropriate credit to the original author(s) and the source, provide a link to the Creative Commons license, and indicate if changes were made. The images or other third party material in this article are included in the article's Creative Commons license, unless indicated otherwise in a credit line to the material. If material is not included in the article's Creative Commons license and your intended use is not permitted by statutory regulation or exceeds the permitted use, you will need to obtain permission directly from the copyright holder. To view a copy of this license, visit <http://creativecommons.org/licenses/by/4.0/>.

© The Author(s) 2017